Materials Advances

ROYAL SOCIETY OF CHEMISTRY

PAPER

View Article Online
View Journal | View Issue

Cite this: *Mater. Adv.*, 2026, 7, 2991

Fe-embedded graphitic carbon nanofibers for efficient urea electrooxidation and stable oxygen reduction reaction in acidic media

Nasser A. M. Barakat [ab]

Fe nanoparticle-incorporated carbon nanofibers (Fe–CNFs) were successfully synthesized *via* electrospinning of a ferrous acetate/PVA solution followed by vacuum drying and calcination at 850 °C. SEM and TEM analyses confirmed the formation of uniform nanofibers containing well-dispersed metallic Fe nanoparticles encapsulated within partially graphitized carbon layers. XRD revealed the presence of crystalline α-Fe together with minor Fe_2O_3 and graphite reflections. Magnetic measurements demonstrated ferromagnetic behavior at both 5 K and 300 K with a clear divergence between ZFC and FC curves, confirming the presence of multi-domain Fe nanoparticles embedded in the carbon matrix. Electrochemically, the Fe–CNFs showed pronounced activation behavior in 1.0 M KOH, where strong Fe(II)/Fe(III) redox peaks in the first cycle diminished upon cycling due to surface reconstruction and the formation of Fe–oxyhydroxide species. Activated fibers exhibited excellent catalytic activity toward urea oxidation, achieving current densities above 120 mA cm^{-2} in 2.0 M urea at 50 mV s^{-1} and demonstrating a negative shift in onset potential with increasing urea concentration. In acidic medium (0.5 M H_2SO_4), the fibers displayed stable capacitive behavior with suppressed Fe redox activity. Remarkably, the Fe–CNFs exhibited strong oxygen reduction reaction activity in acid along with exceptional durability. Additionally, electrospinning directly onto a silicon wafer produced a compact Fe–CNF film (≈7.5 μm thick) strongly fused to the substrate, forming a conductive and mechanically stable coating suitable for integrated electrochemical devices Overall, the results demonstrate that the introduced Fe–CNFs combine robust structural stability, magnetic functionality, and versatile electrocatalytic performance, highlighting their potential as low-cost catalysts for different applications.

Received 10th December 2025,
Accepted 25th January 2026

DOI: 10.1039/d5ma01440a

rsc.li/materials-advances

1. Introduction

Carbon nanofibers (CNFs) have emerged as one of the most versatile one-dimensional carbonaceous materials due to their high electrical conductivity, large surface area, chemical stability, and structural tunability.[1] These attributes make CNFs attractive for diverse applications, including electrocatalysis, environmental remediation, and energy conversion systems.[2] Electrospinning has proven particularly valuable for producing CNFs with controlled morphology and continuous fiber networks, enabling scalable fabrication of carbon nanostructures with uniform microstructures and tailored properties. As concluded by many researchers, electrospinning remains the most effective method for producing polymer-derived nanofibers with diameters ranging from tens to hundreds of nanometers.[3,4]

Incorporating metal nanoparticles into CNFs further enhances their catalytic, electrical, and magnetic properties due to strong metal–carbon interactions and improved electron transport. Metal-incorporated carbon nanofibers have been widely studied for electrocatalytic reactions such as oxygen reduction (ORR),[5] hydrogen evolution (HER),[6] and urea oxidation[7,8] due to the formation of highly dispersed active sites supported on a conductive carbon matrix. However, challenges remain in controlling nanoparticle distribution, preventing aggregation during thermal treatment, and achieving long-term durability under acidic or alkaline electrochemical conditions.

Among earth-abundant metals, iron is especially attractive due to its low cost, environmental compatibility, natural abundance, and well-documented catalytic activity in oxygen reduction, organic oxidation, and wastewater treatment. Fe-based catalysts, including Fe–N–C, Fe_3O_4, and Fe@C composites, have shown promising ORR performance and reasonable

[a] *Chemical Engineering Department, Faculty of Engineering, Minia University, El-Minia, 61516, Egypt. E-mail: nasbarakat@mu.edu.eg; Tel: +0020862321407*
[b] *Chemical Engineering Department, Faculty of Engineering, Atatürk University, 25240, Erzurum, Turkey*

durability.[9,10] However, one major challenge is the intrinsic instability of Fe in acidic electrolyte, where dissolution of Fe^{+2}/Fe^{+3} typically leads to rapid performance degradation, limiting practical applications in proton-exchange membrane (PEM) technologies and acidic electrocatalysis.[11,12] Therefore, strategies to stabilize Fe nanoparticles—especially through encapsulation in graphitic carbon—are crucial for enhancing their long-term performance.

Electrospinning metal–polymer precursor solutions followed by thermal treatment presents an effective approach to embedding metal nanoparticles in a carbon matrix. While metal alkoxides (*e.g.*, titanium isopropoxide) are traditionally used, metal acetates have recently gained attention due to their excellent spinnability, homogeneous dispersion in polymer matrices, and predictable decomposition behavior during carbonization.[13,14] Studies have shown that metal acetates form stable coordination structures that enhance fiber uniformity and facilitate controlled *in situ* formation of metal nanoparticles upon calcination.[15,16] Additionally, iron acetate precursors yield uniformly distributed Fe nanoparticles when carbonized under inert or reducing atmospheres, producing Fe–C composites with improved catalytic and magnetic properties.

Despite extensive work on Fe-based catalysts, several knowledge gaps persist. First, few studies have detailed the complete structural evolution—from precursor to final Fe–CNF—using combined SEM, TEM, XRD, SAED, TGA, and magnetic characterization. Second, the electrocatalytic behavior of Fe–CNFs in both alkaline and acidic media is not well understood, particularly concerning the role of Fe encapsulation in ensuring chemical stability. Third, although Fe dissolution in acid is a well-known limitation, very few reports demonstrate Fe-based materials that retain ORR activity after long-term cycling in strongly acidic electrolytes. Finally, integration of Fe–CNF films directly onto silicon wafers for potential device applications remains underexplored.

In this study, we address these gaps by synthesizing Fe nanoparticle-incorporated carbon nanofibers through electrospinning of ferrous acetate/PVA precursors followed by vacuum calcination at 850 °C. We provide a comprehensive structural analysis correlating nanoparticle formation, carbon graphitization, and magnetic behavior. We further investigate the electrocatalytic performance in alkaline media for urea oxidation and in acidic media for the ORR, where the Fe–CNFs exhibit surprising long-term acid stability attributed to partial graphitic encapsulation of Fe nanoparticles. Additionally, we demonstrate successful deposition of Fe–CNFs directly onto silicon wafers, forming strongly adhered, conductive coatings that broaden the application potential of these nanofibers in integrated electrochemical and microelectronic systems.

2. Materials and methods

2.1 Materials

Poly(vinyl alcohol) (PVA, $M_w \approx 85\,000$–$124\,000$, 99% hydrolyzed), ferrous acetate ($Fe(CH_3COO)_2$, ≥99%), potassium hydroxide (KOH, pellets, ≥85%), sulfuric acid (H_2SO_4, 98%), and urea ($CO(NH_2)_2$, ≥99%) were purchased from Sigma-Aldrich (Germany) and used as received. Isopropanol (IPA, ≥99.5%) was supplied by VWR Chemicals. Nafion® 117 solution (5 wt% in alcohol/water mixture) was obtained from Alfa Aesar and used as an electrochemical binder. Ultrapure deionized water (18.2 MΩ cm) produced by a Milli-Q system (Millipore) was used in all aqueous solution preparations. For electrode preparation, glassy carbon electrodes (GCE, 3 mm diameter, Metrohm), alumina polishing powders (0.05–1.0 μm, Buehler), and carbon tape (Ted Pella) were used. Silicon wafers (single-side polished, n-type, 4-inch diameter) were purchased from University Wafer Inc. and used as substrates for direct electrospinning. All chemicals were of analytical grade and used without further purification.

2.2 Preparation of Fe–nanoparticle-incorporated carbon nanofibers (Fe–CNFs)

Fe–CNFs were synthesized through electrospinning of a ferrous acetate/PVA precursor solution followed by vacuum thermal treatment. First, 15 g of an aqueous PVA solution (10 wt%) was prepared by dissolving PVA granules in deionized water at 80 °C under continuous stirring until a clear and homogeneous solution was obtained. Separately, 1.0 g of ferrous acetate was dissolved in 5 mL of deionized water with mild heating to ensure complete dissolution. The resulting metal–salt solution was added dropwise to the PVA solution and stirred for 5 h at 50 °C to ensure uniform distribution of the metal precursor and to promote coordination between Fe^{2+} ions and the PVA polymer chains. The electrospinning was carried out using a high-voltage power supply (CPS-60 K02V1). The precursor solution was loaded into a 10 mL plastic syringe fitted with a stainless-steel needle. A voltage of 20 kV was applied between the needle tip and a grounded collector, with a tip-to-collector distance of 15 cm and a solution flow rate of 0.8 mL h^{-1}. The nanofibers were collected either on aluminum foil (free-standing nanofiber mats) or directly onto a silicon wafer to obtain substrate-supported CNF films. Electrospinning was conducted at ambient temperature (22–25 °C) and relative humidity of 40–50%. The as-spun nanofiber mats were dried under vacuum at 60 °C for 24 h to remove residual moisture and solvent. Calcination was performed in a tubular furnace under continuous vacuum ($<10^{-2}$ mbar). The temperature was raised to 850 °C at a heating rate of 5 °C min^{-1} and maintained for 2 h.

2.3 Electrochemical measurements

Electrochemical experiments were performed using a standard three-electrode cell connected to a potentiostat/galvanostat (Autolab PGSTAT302N). A glassy carbon electrode (GCE, 3 mm diameter) served as the working electrode, a platinum wire as the counter electrode, and an Ag/AgCl (3 M KCl) electrode as the reference. All potentials in this work are reported *versus* Ag/AgCl unless otherwise stated.

The GCE surface was polished sequentially with 1.0, 0.3, and 0.05 μm alumina slurry, rinsed thoroughly with deionized water, and sonicated in water and ethanol for 2 min to remove

residual particles. A catalyst ink was prepared by dispersing 2.0 mg of Fe–CNFs in a mixture containing 400 μL isopropanol and 20 μL Nafion® 117 solution (5 wt%). The mixture was ultrasonicated for 30 min to form a homogeneous suspension. A 15 μL aliquot of the ink was drop-cast onto the polished GCE surface and dried at room temperature. Prior to electrochemical measurements, the modified electrode was rinsed gently with deionized water to remove any loosely bound material. Activation of the Fe–CNF electrode was carried out in 1.0 M KOH by cycling the potential between −0.2 and 0.8 V at a scan rate of 50 mV s^{-1} for 10–20 cycles. Urea oxidation studies were subsequently performed in 1.0 M KOH containing various concentrations of urea (0.0–2.0 M). Cyclic voltammograms were recorded at a scan rate of 50 mV s^{-1} to evaluate electrocatalytic performance.

The acidic electrochemical response was evaluated in 0.5 M H_2SO_4, where the Fe–CNF electrode was cycled between −0.2 and 0.8 V at 50 mV s^{-1}. Stability tests were conducted by continuously cycling the electrode for 300 cycles at a scan rate of 100 mV s^{-1}. Selected cycles were extracted for comparison to evaluate electrochemical durability. ORR activity was assessed in O_2- and Ar-saturated 0.5 M H_2SO_4. Prior to each measurement, oxygen or argon was bubbled for 10 min to ensure appropriate saturation. CV curves were recorded at a slow scan rate of 5 mV s^{-1} to accurately evaluate the onset potential and ORR kinetics. Catalyst stability toward the ORR was examined by subjecting the electrode to 300 consecutive ORR cycles at 100 mV s^{-1}, after which pre- and post-cycling CV curves were compared. All experiments were conducted at room temperature (22–25 °C). Each measurement was repeated at least three times to confirm reproducibility, and the results were reported as the average of the repeated experiments. Electrochemical data processing was performed using NOVA® software (Metrohm Autolab).

2.4 Characterization techniques

The morphology of the as-spun and calcined nanofibers was examined using scanning electron microscopy (SEM) and field-emission SEM (FE-SEM). Low-magnification SEM images were obtained using a Hitachi S-3400N microscope operating at 5–10 kV, while high-resolution surface imaging was carried out using a JEOL JSM-7600F FE-SEM operated at 5–15 kV. Samples were mounted on carbon tape, and a thin Au/Pd coating (~5 nm) was applied when necessary to reduce charging. For wafer-supported nanofibers, the silicon substrates were cleaved manually, and cross-sectional images were recorded to visualize the adhesion and thickness of the CNF layer.

Further structural analysis was performed using transmission electron microscopy (TEM) on a JEOL JEM-2100 microscope operated at 200 kV. High-resolution TEM (HR-TEM) and selected-area electron diffraction (SAED) were used to investigate particle crystallinity, lattice fringes, and phase distribution. Samples for TEM were prepared by dispersing Fe–CNFs in ethanol *via* ultrasonic agitation followed by drop-casting onto lacey carbon-coated copper grids. Elemental distribution across individual nanofibers was studied using STEM–EDX line-scan mapping integrated with the TEM system.

Crystalline phases present in the samples were identified by X-ray diffraction (XRD) using a PANalytical X'Pert PRO diffractometer equipped with Cu Kα radiation (λ = 1.5406 Å). Patterns were collected over the 2θ range of 10–90° with a step size of 0.020° and an exposure time of 0.5 s per step. The instrument was operated at 40 kV and 40 mA.

Thermogravimetric analysis (TGA) was conducted using a TA Instruments Q500 analyzer to evaluate thermal degradation and carbonization behavior. Approximately 5–10 mg of sample was heated from room temperature to 900 °C at a heating rate of 10 °C min^{-1} under flowing argon (60 mL min^{-1}). First derivative (DTG) curves were generated to interpret multistage mass-loss processes associated with polymer decomposition, precursor breakdown, and final carbon formation.

Magnetic properties of the Fe–CNFs were investigated using a Quantum Design MPMS 3 SQUID magnetometer. Zero-field-cooled (ZFC) and field-cooled (FC) magnetization curves were recorded between 5 K and 350 K under an applied field of 100 Oe to study magnetic transitions and nanoparticle behavior. Magnetic hysteresis loops were measured at both 5 K and 300 K over an applied field range of −30 to +30 kOe to determine coercivity, remanence, and saturation magnetization. Approximately 10 mg of sample was encapsulated in a gelatin capsule, and background correction was applied to eliminate non-magnetic contributions.

The electrical conductivity of the wafer-supported nanofiber films was evaluated using a Keithley 2400 source meter in two-point probe configuration. *I–V* characteristics were collected by sweeping the voltage from −5.0 to +5.0 V while recording the corresponding current. Measurements were repeated at five randomly selected positions on the wafer surface to assess uniformity and reproducibility of the conductive CNF layer.

3. Results and discussion

3.1 Catalyst characterization

3.1.1 Morphology. The morphological features of the as-spun FeAc/PVA nanofibers are shown in Fig. 1A and B. The low-magnification SEM image (Fig. 1A) reveals a well-interconnected fibrous mat composed of uniformly distributed, bead-free nanofibers. Such continuous and defect-free morphology indicates that the FeAc/PVA solution exhibited appropriate viscosity, chain entanglement, and conductivity required for stable electrospinning. At higher magnification (Fig. 1B), the FE-SEM image demonstrates that the individual fibers exhibit smooth surfaces and circular cross-sections, confirming the homogeneity of the precursor solution and the absence of phase separation during jet formation.

The formation of uniform nanofibers from metal–polymer precursor systems strongly depends on the nature of the metal salt. While metal alkoxides (*e.g.*, titanium isopropoxide or zirconium propoxide) are the most frequently employed precursors for electrospinning sol–gel-derived nanofibers, metal

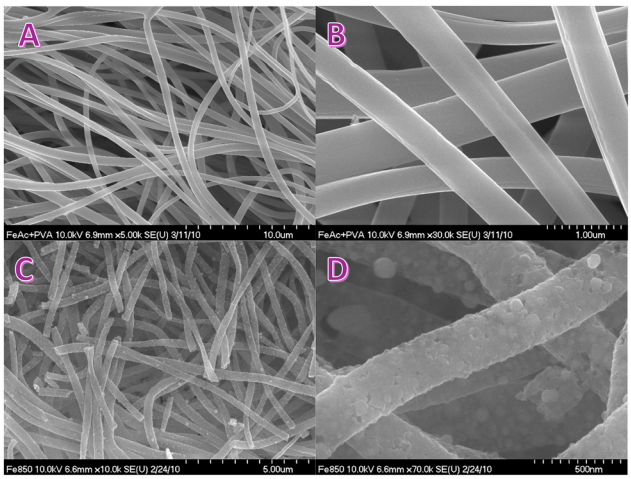

Fig. 1 (A) and (B) SEM and FE-SEM images of the as-spun FeAc/PVA nanofibrous mat showing smooth, continuous, and bead-free fibers with uniform morphology, indicating excellent spinnability of the ferrous acetate/PVA precursor solution. (C) and (D) SEM and FE-SEM images of the nanofibers after calcination at 850 °C under vacuum, demonstrating preservation of the fibrous structure and the formation of surface-decorated iron-based nanoparticles resulting from the thermal decomposition and reduction of ferrous acetate within the carbon matrix.

acetates have also demonstrated excellent spinnability due to their intrinsic polycondensation behavior. This characteristic promotes the formation of extended coordination networks within the polymer matrix, resulting in stable jet elongation and uniform fiber morphology. In several earlier reports, some researchers demonstrated that metal acetates such as nickel acetate, cobalt acetate, and iron acetate lead to exceptionally uniform nanofibers when blended with PVA or PAN, mainly due to the gradual formation of metal–oxygen–carbon clusters that increase solution cohesiveness and prevent bead formation during electrospinning.[17–19]

In the present system, ferrous acetate plays a similar role. The acetate groups undergo partial hydrolysis and polycondensation within the aqueous PVA solution, increasing the viscoelasticity of the jet and facilitating the formation of smooth and continuous fibers. Moreover, the ionic nature of Fe^{+2} enhances the electrical conductivity of the spinning solution, enabling better elongation of the jet and the formation of finer fibers without surface wrinkles or defects. The combination of these effects explains why the FeAc/PVA system successfully produced a highly uniform nanofibrous mat prior to calcination. The SEM observations confirm that ferrous acetate is a suitable precursor for fabricating iron-containing nanofibers through electrospinning, offering morphological advantages comparable to—and often better than—conventional metal alkoxides.

The morphological evolution of the FeAc/PVA nanofibers after calcination at 850 °C under vacuum is shown in Fig. 1C (SEM) and 1D (FE-SEM). The low-magnification image (Fig. 1C) confirms that the fibrous structure is preserved even after high-temperature carbonization, demonstrating the structural robustness of the composite precursor. Despite the significant mass loss associated with decomposition of PVA and ferrous acetate, the nanofibrous network remained intact—without collapse or aggregation. This retention of one-dimensional morphology is consistent with many studies where electrospun polymer/metal–salt composite fibers transform into metal–carbon composite CNFs with maintained fiber morphology after thermal treatment.[20]

At higher magnification (Fig. 1D), the FE-SEM image reveals that the fibers' surfaces are roughened and decorated with uniformly distributed nanoparticles. These surface particles likely correspond to metallic iron (or iron carbide/oxide) species formed *in situ* by decomposition and reduction of ferrous acetate during the vacuum calcination. The granular texture and nanoparticle decoration strongly suggest that the iron precursor was homogenously distributed in the polymer matrix before calcination, facilitating nucleation and growth of iron-based nanoparticles within or on the carbon nanofiber core. This phenomenon—metal nanoparticle formation and surface exposure upon carbonization—has been widely documented in electrospun metal salt/polymer fiber systems.[21]

Moreover, the rough surface and surface-exposed nanoparticles imply that the carbon matrix contracted during pyrolysis, possibly due to PVA decomposition and carbon densification, causing the metal clusters to migrate or be "pushed out" toward the fiber surface as the carbon matrix shrank. Such internal rearrangement during carbonization is frequently observed in polymer-derived CNFs, especially when transition-metal salts are used as precursors, because the evolving carbon matrix exerts compressive forces as volatile byproducts are removed.

The successful preservation of fiber morphology with embedded (or surface-anchored) metal nanoparticles underscores the suitability of using metal acetates like ferrous acetate as precursors in electrospun fibers destined for CNF production. As noted in comprehensive reviews, the electrospinning technique followed by carbonization remains one of the most effective and versatile methods for generating CNFs with metal or metal–oxide functionalities for applications such as catalysis, energy storage, or sensing.[22] These morphological features suggest that the electrospinning + vacuum-calcination route is effective for producing Fe NP-decorated CNFs with well-controlled architecture—a promising platform for further structural, compositional, and functional characterization.

3.1.2 Chemical composition. The crystalline phases of the calcined FeAc/PVA nanofibers were examined using XRD, and the resulting diffraction pattern is presented in Fig. 2A. The pattern is dominated by several intense and well-defined peaks located at $2\theta \approx 44.7^\circ$, 65.1°, 82.4°, and 98.9°, which correspond to the (110), (200), (211), and (220) reflections, respectively, of body-centered cubic (bcc) α-Fe, as indexed to JCPDS card No. 06-0696. The prominence of the (110) peak indicates preferential orientation or higher crystallinity along this plane, which is commonly observed for Fe nanoparticles synthesized under reducing or low-oxygen conditions. The presence of these peaks confirms that metallic Fe^0 nanoparticles were successfully generated during the vacuum calcination of the ferrous acetate/PVA composite fibers at 850 °C. Formation of zerovalent

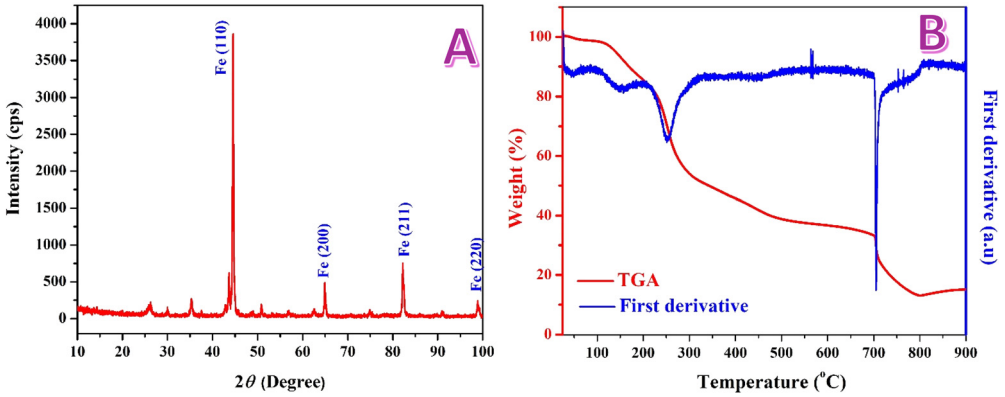

Fig. 2 (A) XRD pattern of the calcined FeAc/PVA nanofibers showing characteristic diffraction peaks of metallic α-Fe (JCPDS 06-0696) along with minor reflections corresponding to Fe_2O_3 (JCPDS 39-1346) and a broad peak near 25° associated with turbostratic graphitic carbon (JCPDS 41-1487). (B) TGA and first-derivative (DTG) curves of the FeAc/PVA precursor nanofibers.

iron can be attributed to the abnormal thermal decomposition of the acetate anion. It was concluded that hydrogen and carbon monoxide gases are evolved during the decomposition process which resulted in complete reduction of the iron ions to the obtained zerovalent state.[15,16]

In addition to the characteristic Fe reflections, several low-intensity peaks are also observed at $2\theta \approx 30.3^\circ$, 35.7°, 43.3°, 57.3°, and 63.1°, corresponding to the (220), (311), (400), (511), and (440) planes of Fe_2O_3 (hematite), as referenced by JCPDS card no. 39-1346. These weak features indicate the presence of trace iron oxide species, which may originate from limited oxidation of the Fe nanoparticles either during heating or exposure to ambient air after calcination. Such mixed-phase formation (Fe^0 with minor Fe_2O_3) is commonly reported for Fe-based CNFs derived from metal acetates, as partial oxidation of surface Fe atoms is often unavoidable even under vacuum conditions.

Furthermore, a broad and weak diffraction hump centered around $2\theta \approx 24$–26° corresponds to the (002) plane of turbostratic carbon, consistent with the presence of graphitic domains (JCPDS card no. 41-1487). The observed broadness of this peak suggests the formation of partially ordered or defective graphitic carbon, which aligns with the catalytic role of iron in promoting graphitization of the carbon matrix at elevated temperatures. Transition metals such as Fe are known to act as graphitization catalysts, facilitating reordering of PVA-derived carbon into stacked graphene-like layers during high-temperature treatment, a phenomenon well documented in carbon nanofiber systems.

The thermal behavior of the FeAc/PVA electrospun nanofibers was investigated using TGA coupled with first-derivative (DTG) analysis, as presented in Fig. 2B. The TGA curve shows three major weight-loss regions, each corresponding to well-defined decomposition steps associated with moisture removal, polymer degradation, and decomposition of ferrous acetate.

The initial weight loss occurring below ~150 °C is relatively small and is attributed to the evaporation of physically adsorbed water and residual solvent molecules entrapped within the nanofiber network. This behavior is typical for hydrophilic polymers such as PVA, which readily absorb moisture from the environment.

A more prominent weight-loss stage is observed between approximately 200 and 350 °C, accompanied by a sharp DTG peak, indicating the main degradation step of the PVA matrix. In this region, PVA undergoes dehydration, chain scission, and elimination reactions leading to the formation of polyene residues and the evolution of volatile organic products. This degradation behavior is consistent with earlier thermal studies of PVA-based electrospun fibers, which typically show a major decomposition event in the same temperature range.

The gradual mass loss observed between 350 and 600 °C corresponds to the thermal decomposition of ferrous acetate. Ferrous acetate is known to decompose through a series of intermediate steps, including the formation of iron carbonate and iron oxide species, followed by reduction to metallic iron under an inert atmosphere due to the presence of the aforementioned reducing gases. This multistep transformation is reflected in the broad DTG signal within this temperature region. During this stage, gaseous products such as CO_2, CO, and acetic acid are released, contributing to the overall weight loss.

A final and sharp DTG event is seen around ~700–750 °C, marking the transition from intermediate iron species to stable metallic Fe^0 nanoparticles and, simultaneously, the carbonization of the remaining polymer backbone. Vacuum calcination at temperatures near 850 °C promotes the conversion of PVA-derived carbon into a partially graphitized structure, while the iron species act as catalysts for carbon ordering. This is consistent with the XRD results confirming the presence of metallic Fe and graphitic carbon. Beyond ~750 °C, the TGA curve stabilizes, indicating that the system reaches thermal equilibrium and no further significant mass loss occurs.

3.1.3 Internal structure. The internal structure and nanoparticle distribution within the calcined FeAc/PVA nanofibers were further examined by TEM, as shown in Fig. 3A and B. The low-magnification image in Fig. 3A clearly reveals that the nanofibers contain a high density of dark nanoparticles embedded along the entire length of the carbon matrix. These

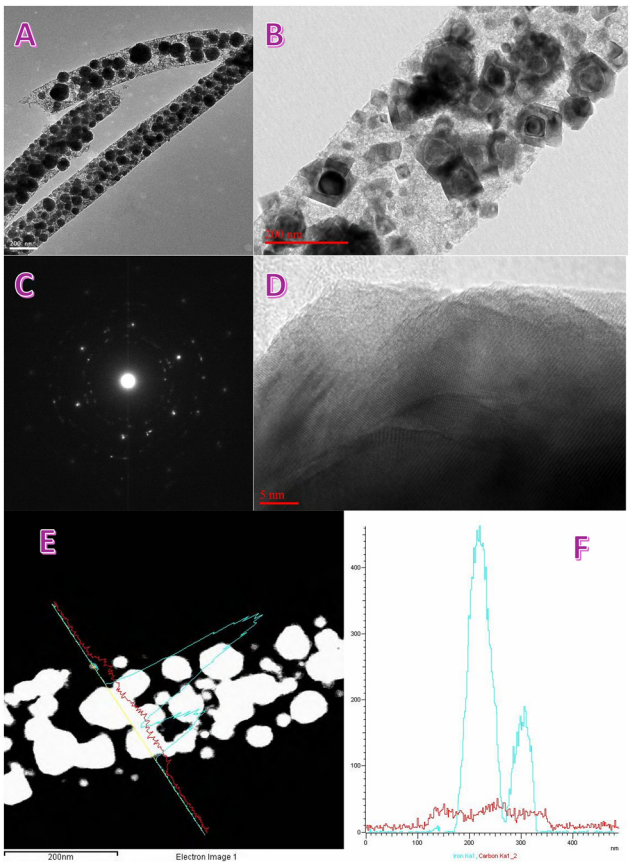

Fig. 3 (A) and (B) TEM images of the calcined FeAc/PVA nanofibers showing a high density of iron-based nanoparticles uniformly distributed along the carbon nanofiber matrix. (C) SAED pattern displaying distinct diffraction rings corresponding to the (110), (200), and (211) planes of metallic α-Fe, confirming the polycrystalline nature of the Fe nanoparticles. (D) HR-TEM image revealing well-defined lattice fringes assigned to α-Fe and partially graphitized carbon layers surrounding the nanoparticles. (E) TEM line-scan mapping performed across a randomly selected region of the nanofiber, highlighting Fe-rich nanoparticle domains. (F) Corresponding elemental intensity profile for Fe and C along the scanned line, demonstrating strong localized Fe peaks embedded within a continuous carbon matrix.

nanoparticles appear well-distributed, forming a continuous Fe-rich architecture within the carbon nanofibers, confirming that ferrous acetate was homogeneously incorporated within the polymer precursor before calcination. Such uniform internal decoration is characteristic of metal–acetate-derived CNFs and directly reflects the molecular-level mixing achieved during the electrospinning process.

At higher magnification (Fig. 3B), the nanoparticles exhibit distinct crystallinity and well-defined shapes, including spherical and polyhedral morphologies. The observable lattice contrast and sharp particle boundaries indicate the successful formation of crystalline Fe-based nanoparticles during the vacuum calcination at 850 °C. These observations are fully aligned with the XRD results (Fig. 2A), which confirmed the presence of metallic α-Fe as the dominant crystalline phase, accompanied by trace Fe_2O_3. The bright–dark contrast of the images and the relatively uniform particle size also support the conclusion that Fe^0 nanoparticles were generated *in situ via* the thermal decomposition and reduction of ferrous acetate.

The TEM findings further reveal that the nanoparticles are strongly anchored within the carbon nanofiber matrix rather than loosely attached to the surface. This suggests that nucleation of Fe particles occurred internally during carbonization, followed by limited outward migration of some nanoparticles driven by matrix shrinkage—an effect commonly reported in electrospun metal–polymer composite systems. The encapsulating or partially embedded nature of the Fe nanoparticles is advantageous, as it enhances the structural stability of the CNFs and creates intimate metal–carbon interfaces known to improve catalytic and electrochemical performance.

Overall, the TEM analysis confirms the successful synthesis of Fe-incorporated carbon nanofibers with uniformly dispersed, crystalline iron nanoparticles embedded throughout the carbon framework. These results, when considered alongside the XRD data, unequivocally demonstrate the formation of a multiphase Fe–CNF structure consisting of metallic iron nanoparticles supported on a partially graphitized carbon matrix.

The SAED pattern of the calcined nanofibers (Fig. 3C) exhibits a set of bright diffraction rings along with discrete spots, indicating the presence of polycrystalline iron-based nanoparticles within the carbon matrix. The positions of the diffraction rings correspond well with the major lattice planes of metallic α-Fe identified by XRD (Fig. 2A). In particular, the rings observed at radii matching the (110), (200), and (211) planes confirm the formation of crystalline body-centered cubic (bcc) Fe nanoparticles (JCPDS 06-0696). The appearance of sharp spots superimposed on the rings suggests that some Fe nanoparticles exhibit a higher degree of crystallinity and larger grain size, consistent with the crystalline features observed in the TEM images.

The HR-TEM micrograph (Fig. 3D) further substantiates these findings by displaying well-defined lattice fringes with interplanar spacings matching the characteristic planes of metallic Fe. The measured *d*-spacing values are consistent with the (110) or (200) reflections of α-Fe, confirming that the nanoparticles are predominantly metallic, in full agreement with the XRD analysis. Additionally, the surrounding carbon matrix exhibits stacked, yet turbostratic graphitic layers, which appear partially ordered. This structural arrangement is typical for polymer-derived carbon nanofibers treated at high temperatures and is further enhanced by the catalytic graphitization effect of Fe, which accelerates the reorganization of amorphous carbon into layered graphene-like structures during calcination.

The coexistence of crystalline Fe nanoparticles and graphitized carbon layers indicates strong metal–carbon interactions formed during thermal decomposition of ferrous acetate. This interaction results in embedded or partially encapsulated Fe nanoparticles stabilized within the carbon matrix, as also evidenced in the TEM images (Fig. 3A and B). The structurally integrated Fe–carbon architecture is beneficial for catalytic and electrochemical applications because it provides robust electron-transport pathways, highly active surface areas, and

strong anchoring of metal nanoparticles that minimizes aggregation during operation.

To further verify the spatial distribution of iron within the calcined nanofibers, line-scanning elemental mapping was performed across a randomly selected region of the Fe–CNFs, as shown in Fig. 3E. The corresponding intensity profile for Fe and C along the scanned line is presented in Fig. 3F. The elemental profile reveals distinct and well-defined peaks for Fe, which align with the bright nanoparticle-rich regions observed in the TEM image. This confirms that the bright contrast features correspond to iron-containing nanoparticles embedded within or protruding from the carbon nanofiber matrix.

The Fe signal exhibits strong, localized maxima, indicating that iron is concentrated within discrete nanoparticle domains rather than being uniformly dispersed at the atomic level across the carbon structure. This observation is consistent with the TEM and HR-TEM results, which showed the presence of well-defined, crystalline Fe nanoparticles distributed along the fiber length. Moreover, the sharp Fe peaks in the line profile reflect the relatively large size and high concentration of metallic Fe nanoparticles, supporting the XRD conclusion that α-Fe is the dominant crystalline phase formed during vacuum calcination at 850 °C.

In contrast, the carbon signal displays a more uniform and lower-intensity profile, consistent with the continuous amorphous-to-turbostratic carbon matrix that forms the structural backbone of the nanofibers. The broad and relatively steady C baseline indicates that carbon surrounds the Fe nanoparticles, providing a stable support structure that prevents sintering and aggregation during high-temperature treatment. This complementary distribution of Fe and C strongly suggests that iron nanoparticles are well anchored within the carbon matrix—an architecture highly desirable for catalytic and electrochemical applications due to enhanced electron transfer and mechanical stability.

Taken together, the line mapping and elemental distribution results further validate the successful formation of Fe-incorporated CNFs, with iron nanoparticles uniformly distributed along the fiber structure and embedded within a partially graphitized carbon network. These findings are in full agreement with the structural characterization provided by XRD, TGA, TEM, and SAED.

3.2 Immobilization on the Si substate

To explore the potential for device-level integration, the electrospinning process was performed using a polished silicon wafer as the direct collector for the FeAc/PVA nanofibers. After deposition, the wafer–fiber assembly was dried and calcined under the same vacuum and temperature conditions (850 °C) used for free-standing fiber mats. This produced a conductive Fe–CNF coating strongly bonded to the silicon substrate.

The SEM image (Fig. 4A) shows a uniform and dense network of Fe–CNFs fully covering the wafer surface. The nanofibers retained their 1D morphology, forming an interconnected conductive film. The fiber density is comparable to the

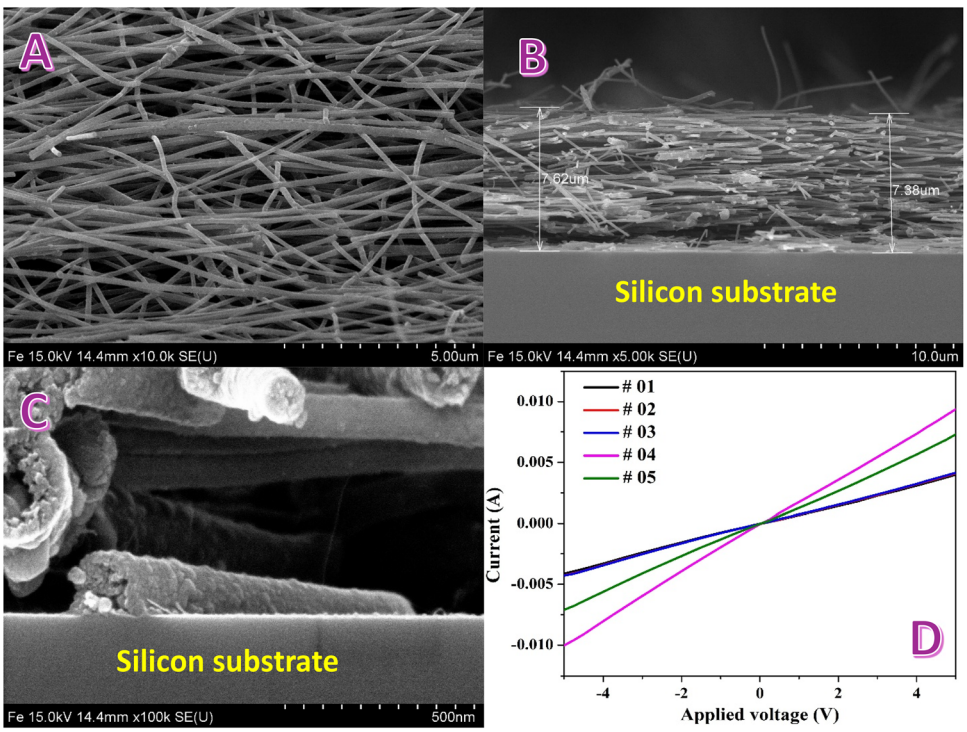

Fig. 4 (A) SEM image of the silicon wafer surface after electrospinning and calcination, showing a uniform and dense coating of Fe–CNFs. (B) Cross-sectional SEM image of the coated wafer displaying a continuous nanofiber layer with an average thickness of ~7.4–7.6 μm adhered strongly to the silicon substrate. (C) High-magnification FE-SEM image revealing the fusion of the lower Fe–CNF layers with the silicon surface. (D) *I*–*V* curves measured at five random positions on the coated wafer, demonstrating uniform ohmic behavior and confirming the formation of a continuous conductive Fe–CNF film on the silicon substrate.

free-standing mats, indicating that the presence of a rigid substrate did not hinder electrospinning jet stability or fiber deposition.

The cross-sectional SEM image (Fig. 4B) reveals that the nanofiber film is approximately 7.4–7.6 μm thick and is firmly attached to the silicon wafer. The layered stacking of fibers is visible, and the film thickness is consistent along the scanned region of the substrate. The preservation of the fibrous architecture confirms that calcination did not cause collapse or severe shrinkage of the deposited layer.

The high-magnification FE-SEM image (Fig. 4C) shows partial fusion or anchoring of the lower nanofiber layers with the silicon substrate. Several mechanisms may contribute to this strong adhesion:

(1) Formation of silicon carbide (SiC) at the interface

• At 850 °C and in a vacuum environment, direct carbon–silicon reactions can occur, particularly if carbon is present in a reactive form (amorphous carbon or carbon radicals from PVA decomposition).[23]

• The reaction Si + C → SiC is thermodynamically favorable above ∼700–800 °C under low-oxygen environments.[24]

• This can produce an ultrathin SiC interfacial layer, improving bonding between the carbonized nanofibers and the silicon.

(2) Diffusion bonding *via* metallic Fe nanoparticles

• Fe nanoparticles have a strong affinity for silicon and can form Fe–Si intermetallic phases at elevated temperatures.[25]

• Localized diffusion of Fe into the native silicon oxide layer or interfacial Si may create Fe–Si bonding regions that anchor the fibers to the surface.[26]

(3) Partial softening or decomposition of the native SiO_2 layer

• The native oxide on silicon can undergo structural modification under vacuum at 850 °C, making it more reactive toward carbon species or Fe nanoparticles.[27]

• This enables mechanical interlocking or chemical bonding of the nanofiber layer to the substrate.

The combined effects likely lead to the observed strong adhesion between the Fe–CNF layer and the silicon wafer.

Electrical *I–V* measurements taken at five different locations on the coated wafer (Fig. 4D) demonstrate linear ohmic behavior, confirming that the Fe–CNF layer is uniformly conductive. The slight variations in slope (conductivity) among the measurement points may result from: local differences in fiber density, variations in nanoparticle concentration, or differences in film thickness. The overall consistent ohmic response indicates that the Fe–CNF layer forms a continuous conductive network suitable for potential microelectronic, sensing, or heating applications.

The results confirm that the electrospun Fe–CNF film can be directly synthesized on a silicon wafer, strongly bonded through chemical and thermal interfacial mechanisms, while maintaining excellent electrical conductivity. This substrate-integrated architecture opens the door for: (1) miniaturized electrochemical devices, (2) on-chip sensors, (3) microheaters, and (4) integrated catalytic platforms.

3.3 Magnetic properties

The magnetic behavior of the Fe-incorporated carbon nanofibers was investigated using temperature-dependent magnetization (ZFC–FC) and magnetic hysteresis measurements. The ZFC and FC curves, presented in Fig. 5A, exhibit features characteristic of ferromagnetic metal nanoparticles embedded within a carbon matrix. The ZFC magnetization increases steadily with temperature, beginning from approximately 0.8 emu g^{-1} at room temperature and rising up to nearly 1.35 emu g^{-1} at 350 °C. This continuous increase reflects the progressive thermal activation of blocked magnetic domains; as temperature rises, thermal energy enables a greater fraction of Fe nanoparticles to overcome their anisotropy barriers and align more effectively with the applied field.[28] The broadness of the ZFC response and the absence of a sharp blocking temperature indicate the existence of a wide particle size distribution and significant interparticle magnetic interactions, both of which

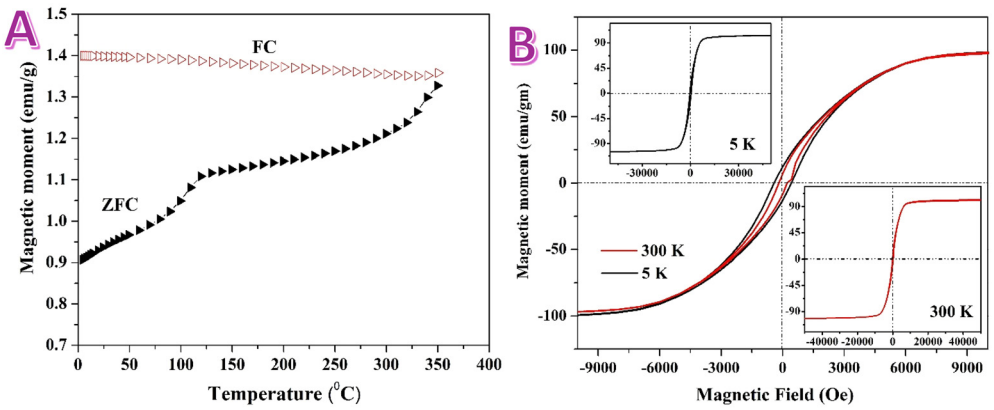

Fig. 5 (A) Zero-field-cooled (ZFC) and field-cooled (FC) magnetization curves of the Fe-incorporated carbon nanofibers, showing the characteristic divergence associated with ferromagnetic Fe nanoparticles embedded within the carbon matrix. (B) Magnetic hysteresis loops measured at 5 K and 300 K. The inset loops highlight the significant coercivity at 5 K and the reduced coercivity at 300 K, demonstrating ferromagnetic behavior at both temperatures.

are supported by TEM observations showing variably sized Fe nanoparticles dispersed throughout the nanofiber structure.

The FC magnetization curve, in contrast, remains nearly constant across the entire temperature range, showing only a slight increase at higher temperatures. This behavior is characteristic of ferromagnetic systems in which magnetic domains, once aligned under a cooling magnetic field, remain stable due to strong magnetic anisotropy.[29] The clear divergence between ZFC and FC curves confirms the dominance of ferromagnetic α-Fe nanoparticles and indicates that the system is not superparamagnetic at room temperature. The thermal stability of the magnetic response up to 350 °C further supports the presence of metallic Fe nanoparticles formed during calcination under vacuum at 850 °C.

The magnetic hysteresis loops shown in Fig. 5B provide additional insight into the magnetic state of the material at low and high temperatures. At 5 K, the M–H curve displays a nearly square hysteresis loop with high saturation magnetization and significant coercivity, typical of ferromagnetic materials with strong anisotropy at low temperatures. This is consistent with the presence of crystalline α-Fe nanoparticles of tens of nanometers in size, as confirmed by HR-TEM and XRD analyses. At 300 K, the hysteresis loop becomes narrower and shows reduced coercivity, although the material clearly remains ferromagnetic. The decrease in coercivity from 5 K to 300 K reflects the thermal activation of magnetic domains, which enhances magnetic relaxation and domain-wall mobility at ambient temperature. The persistence of hysteresis at 300 K demonstrates that the Fe nanoparticles are larger than the superparamagnetic limit and retain stable magnetic ordering under ambient conditions.[30]

The magnetic behavior observed in these Fe–CNFs closely resembles that of other iron–carbon nanocomposites reported in the literature. For example, Fe@C nanofibers derived from polymer electrospinning and Fe-filled carbon nanotubes both exhibit strong FC–ZFC divergence, robust room-temperature ferromagnetism, and similar reductions in coercivity with increasing temperature. These characteristics are typical of α-Fe nanoparticles embedded in a conductive carbon matrix, where the carbon shell or framework restricts nanoparticle migration and prevents oxidation, thereby preserving metallic Fe even under elevated temperatures. The saturation magnetization values observed here ($\sim$100 emu g^{-1} normalized to Fe content) fall within the expected range for Fe-based composites, further confirming the successful formation of metallic α-Fe nanoparticles within the CNF matrix.

In summary, the combined ZFC–FC and hysteresis data unambiguously demonstrate that the Fe-incorporated CNFs exhibit thermally stable ferromagnetism, with strong domain interactions and robust magnetic ordering from cryogenic temperatures up to well above room temperature. This magnetic stability, coupled with the electrically conductive carbon framework, highlights the potential of these materials for magnetically assisted catalysis, electromagnetic shielding, microwave absorption, and device-integrated magnetic components.

3.4 Electrochemical activity

3.4.1 In alkaline medium, urea electrooxidation. The electrochemical activation of the Fe-incorporated carbon nanofibers was first evaluated using cyclic voltammetry in 1.0 M KOH (Fig. 6A). During the initial activation cycle, pronounced redox peaks appear in the potential range of approximately 0.4–0.8 V *vs.* Ag/AgCl, reflecting the presence of surface-accessible Fe species undergoing Fe(II)/Fe(III) transitions. These intense redox signatures diminish progressively over subsequent cycles, indicating rapid surface restructuring of the Fe nanoparticles. As shown in Fig. 6B, the magnitude of the anodic and cathodic peaks decreases markedly between cycles 1, 4, and 10, eventually leading to a more stable voltammetric profile.

This behavior is consistent with widely reported activation processes of Fe-based electrodes in alkaline media, where the initial cycling promotes partial oxidation of metallic Fe to FeOOH or Fe_2O_3, the formation of mixed $Fe(OH)_x$ layers, and the removal of loosely bound surface species. Such transformations reduce the number of electrochemically accessible Fe redox sites, leading to diminished peak intensities in later cycles. Similar effects have been reported for Fe–C composites, Ni–Fe catalysts, and Fe-based oxides, where the activation process involves a transition from a metal-rich surface to a more stable oxide/hydroxide layer.[31,32] The stabilization of the CV response indicates that the electrode surface reaches a quasi-equilibrium state suitable for catalytic measurements.

Following activation, the Fe–CNFs were evaluated for urea electrooxidation in alkaline medium at a scan rate of 50 mV s^{-1} (Fig. 6C). The voltammograms obtained in KOH containing 0.0, 0.5, and 2.0 M urea clearly show that the presence of urea significantly enhances the anodic current density. In pure 1.0 M KOH (0.0 M urea), the electrode exhibits only a small anodic response, attributable primarily to surface hydroxylation and minor Fe-related redox activity. Upon introduction of 0.5 M urea, the anodic current increases substantially and the onset potential for oxidation shifts negatively, demonstrating the catalytic role of Fe-derived oxyhydroxide species in promoting urea oxidation. When the urea concentration is increased to 2.0 M, the current density rises further and reaches values exceeding 120 mA cm^{-2}, indicating strong catalytic activity and efficient utilization of the active surface.

The enhancement in urea oxidation with increasing concentration reflects both improved mass transport and higher reaction kinetics facilitated by FeOOH/Fe–OH active sites generated during the activation step. This behavior is in agreement with other Fe-containing catalysts, where *in situ*-formed FeOOH and Fe(III) species act as electrophilic centers for the oxidative decomposition of urea molecules.[33] The negative shift in onset potential and the substantial increase in oxidation current observed here are comparable to Fe-doped carbon dots,[34] Fe–Ni oxyhydroxides,[35] and Fe-supported carbonaceous[36] materials previously reported as promising catalysts for alkaline urea electrooxidation.

3.4.2 In acidic medium. The electrocatalytic activity of the Fe-incorporated carbon nanofibers was further evaluated in acidic medium using cyclic voltammetry in 0.5 M H_2SO_4 at a

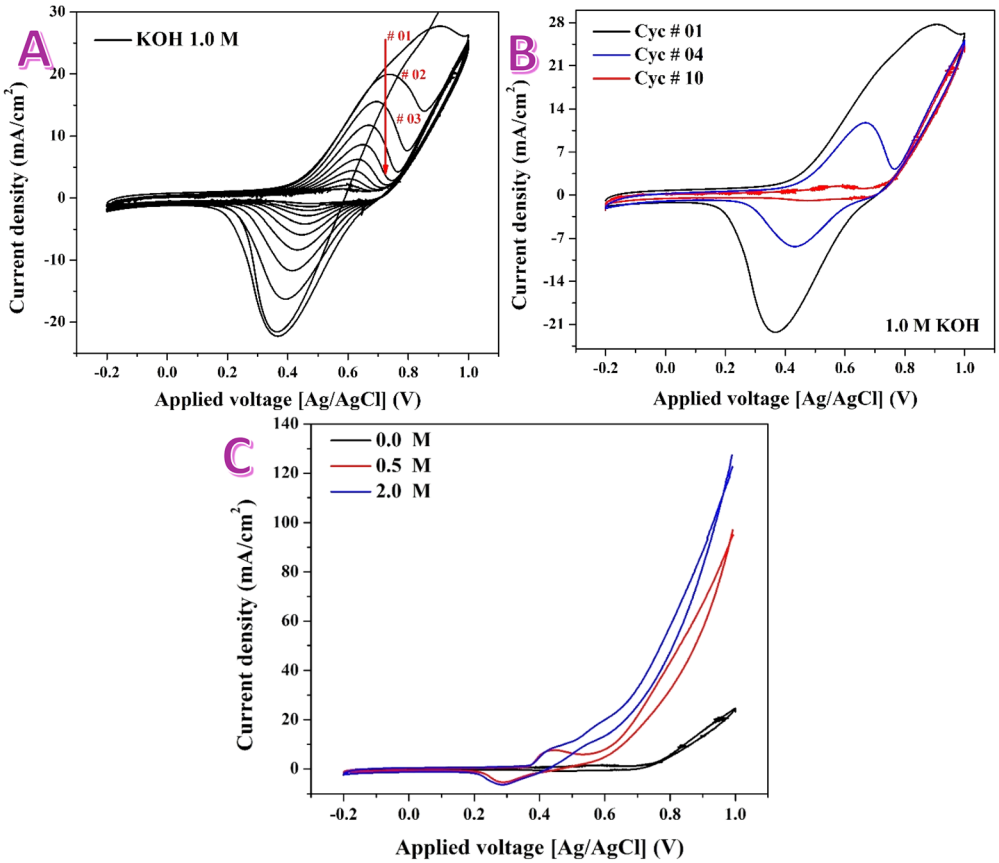

Fig. 6 (A) Cyclic voltammetry activation cycles of Fe–CNFs in 1.0 M KOH (scan rate: 50 mV s^{-1}), showing strong Fe-related redox peaks in the first cycle that gradually decrease in intensity. (B) Selected CV cycles (#1, #4, and #10) highlighting the rapid attenuation of the Fe(II)/Fe(III) redox features and stabilization of the electrode surface upon successive cycling. (C) CV curves of the activated Fe–CNFs in 1.0 M KOH containing different urea concentrations (0.0, 0.5, and 2.0 M in 1.0 M KOH), demonstrating a significant increase in anodic current density and a negative shift in onset potential with higher urea concentrations, confirming enhanced catalytic activity toward urea electrooxidation.

scan rate of 50 mV s^{-1}. As shown in Fig. 7A, the overall voltammetric response exhibits a predominantly capacitive profile with relatively low faradaic contribution, indicating that the Fe–CNF surface remains largely electrochemically stable but does not undergo significant redox transformations in acidic electrolyte. Unlike the behavior observed in 1.0 M KOH, where pronounced Fe(II)/Fe(III) redox peaks appear during activation, the acidic medium suppresses most Fe redox transitions due to the intrinsic instability of iron oxyhydroxide species under strongly acidic conditions.

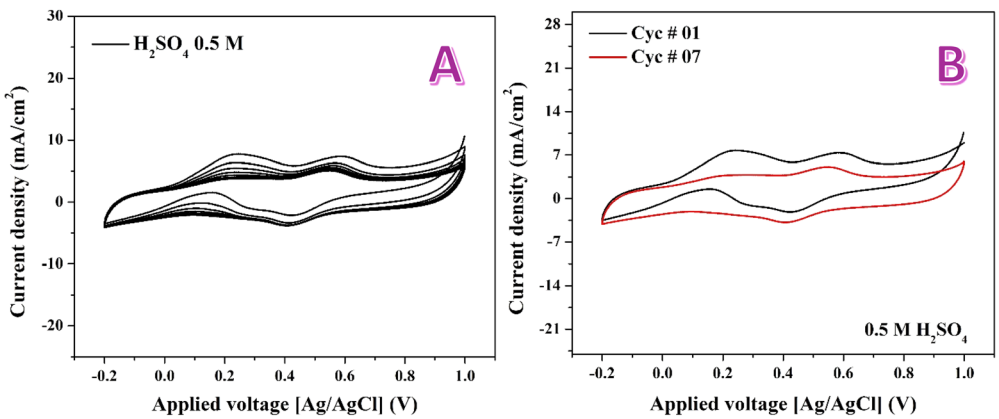

Fig. 7 (A) Cyclic voltammetry (CV) curves of the Fe–CNFs in 0.5 M H_2SO_4 at a scan rate of 50 mV s^{-1}, showing a predominantly capacitive response with limited faradaic activity and gradual stabilization over successive cycles. (B) Selected CV cycles highlighting the slight decrease in current density during the initial sweeps.

During the successive cycling in 0.5 M H_2SO_4, the CV curves gradually stabilize, as displayed in both the full cycle set (Fig. 7A) and the selected cycles (Fig. 7B). The slight decrease in current density over the initial cycles suggests mild surface modifications or partial dissolution of exposed Fe nanoparticles, consistent with the known corrosion susceptibility of Fe in acidic media. Once the Fe-containing surface layer undergoes dissolution or passivation, the voltammetric response becomes more repeatable, controlled primarily by the capacitive behavior of the underlying carbon nanofiber matrix.

This behavior aligns well with previous studies reporting that Fe nanoparticles and Fe-based catalysts exhibit limited redox activity in acidic solutions due to the preferential dissolution of Fe^{+2}/Fe^{+3} species and the inability of iron oxyhydroxides to remain stable at low pH. As a result, Fe-based electrodes in acidic environments often show suppressed redox signatures and reduced catalytic activity compared with their performance in alkaline media.

The absence of significant anodic or cathodic peaks also confirms that urea oxidation or oxygen evolution reaction (OER)-like processes do not proceed efficiently under acidic conditions with Fe-based catalysts. This further highlights the strong pH dependence of Fe electrocatalysis, with alkaline media providing far more favorable conditions for Fe–OOH formation, electron-transfer kinetics, and catalytic oxidation.

Overall, the Fe–CNFs display stable and reproducible behavior in 0.5 M H_2SO_4 but with limited faradaic activity due to Fe dissolution and suppression of Fe redox transitions. These findings clearly indicate that the prepared Fe–CNFs are more electrochemically active and catalytically relevant in alkaline environments than in acidic ones, consistent with established behavior of Fe-based electrocatalysts.

The oxygen reduction reaction (ORR) activity of the Fe-incorporated carbon nanofibers was evaluated in 0.5 M H_2SO_4 under both Ar- and O_2-saturated conditions. As shown in Fig. 8A, the voltammetric response at 5 mV s^{-1} reveals a clear enhancement in cathodic current in the presence of O_2, confirming the catalytic ability of the Fe–CNFs toward the ORR. The characteristic cathodic wave observed under O_2 bubbling indicates activation of oxygen adsorption and electron-transfer processes at the Fe–carbon interface. Such behavior is typical for Fe–N–C and Fe–C catalysts, where iron centers embedded in a conductive carbon matrix facilitate the ORR through a combination of direct O_2 reduction and surface-bound peroxide pathways.[37–39] Compared with the Ar-saturated condition, the cathodic current increases significantly upon O_2 introduction,

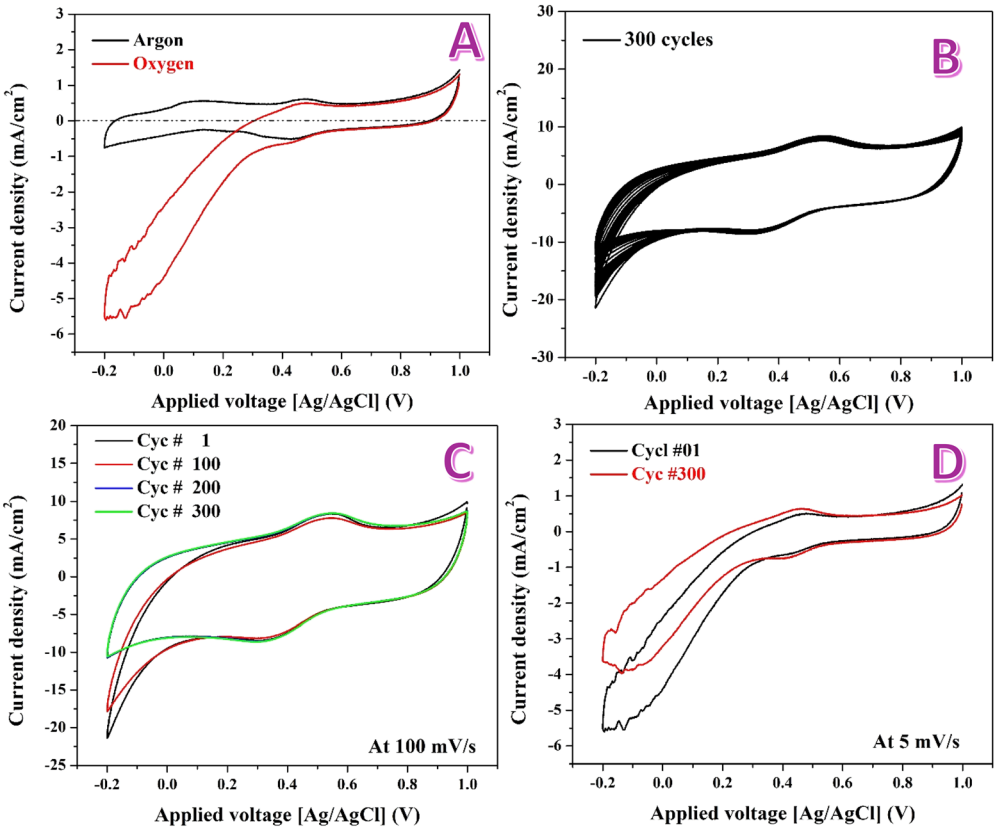

Fig. 8 (A) Cyclic voltammograms of Fe–CNFs recorded in 0.5 M H_2SO_4 at 5 mV s^{-1} under Ar- and O_2-saturated conditions. (B) Continuous cycling of the Fe–CNF electrode in O_2-saturated electrolyte for 300 cycles at 100 mV s^{-1}, demonstrating excellent electrochemical durability with minimal change in current density. (C) Selected CV curves (cycles #1, #100, #200, and #300) illustrating the strong overlap between cycles 200 and 300. (D) Comparison of CV curves at 5 mV s^{-1} before and after the 300-cycle durability test, showing only slight changes in ORR activity, confirming the remarkable acid stability of the Fe–CNFs, attributed to carbon encapsulation and strong metal–carbon interactions.

indicating a high density of active sites and appropriate wetting of the nanofiber surface. The slight positive shift of the ORR onset potential further confirms that the Fe-containing surface undergoes a stable redox behavior despite the acidic environment.

The electrochemical durability of Fe–CNFs was assessed by subjecting the electrode to 300 successive CV cycles in O_2-saturated 0.5 M H_2SO_4 at 100 mV s^{-1} (Fig. 8B). The CV curves show minimal change in both cathodic and anodic current densities across all cycles, demonstrating exceptional electrochemical stability. Selected curves (Fig. 8C) show that cycles 200 and 300 almost completely overlap, confirming the structural and catalytic robustness of the Fe–CNFs. The observed durability is particularly noteworthy, as metallic Fe is typically unstable in acidic environments due to dissolution and corrosion. Iron nanoparticles normally undergo rapid degradation in acidic ORR testing, as widely reported for Fe-based catalysts. Thus, the unusually high stability observed here indicates that the Fe nanoparticles are protected within a carbon matrix.

Although Fe metal is known to be acid-sensitive, the Fe nanoparticles in these CNFs are remarkably stable due to the unique structural features imparted during electrospinning and vacuum calcination:

(1) Encapsulation of Fe nanoparticles within graphitic carbon layers: HRTEM (Fig. 3D) shows partially graphitized carbon surrounding Fe nanoparticles. Graphitized carbon acts as a protective shell that prevents direct contact between Fe and the acidic electrolyte. Encapsulation of Fe in graphitic carbon has been reported to significantly enhance resistance to corrosion under acidic ORR conditions.

(2) Strong metal–carbon interfacial bonding: vacuum calcination at 850 °C promotes Fe–C interactions, producing embedded metal sites that are less susceptible to dissolution. Studies on Fe@C structures show that Fe embedded within carbon matrices exhibits much higher chemical stability than unsupported nanoparticles.[40]

(3) Limited exposure of Fe to electrolyte due to fiber morphology: TEM and SEM analyses confirm that Fe nanoparticles are distributed throughout the fiber volume, not exclusively on the surface. Only a fraction of Fe is exposed, reducing the effective dissolution rate.

(4) Possible formation of ultra-thin Fe–O–C protective layers: electrochemical activation may lead to the formation of thin Fe–oxy species that stabilize the Fe/carbon interface without promoting extensive dissolution, similar to behavior observed in Fe–N–C ORR catalysts.[41]

These combined protective effects explain why Fe–CNFs show unusually high stability, even during prolonged ORR cycling in acidic medium.

The CV curves at 5 mV s^{-1} before and after 300-cycle durability testing (Fig. 8D) show only a slight decrease in cathodic current, with nearly identical curve morphology. This confirms that the structural integrity and catalytic functionality of the Fe–CNFs remain essentially unchanged after extended cycling, further supporting the strong encapsulation and protection mechanisms discussed above. The retention of ORR activity after aggressive cycling conditions highlights the practical potential of Fe–CNFs for acidic electrochemical applications—a domain where Fe-based catalysts typically suffer rapid deactivation.

Finally, it is worth emphasizing that the present study is not primarily intended as a benchmarking exercise against previously reported Fe-based electrocatalysts, but rather as a materials-oriented investigation introducing a distinct Fe nanoparticle–embedded carbon nanofiber system with unique structural and functional attributes. In contrast to many Fe-based catalysts that focus solely on activity optimization, the Fe–CNFs reported here combine multiple uncommon features, including derivation from a metal acetate precursor, strong graphitic encapsulation of Fe nanoparticles, and direct immobilization onto silicon substrates to form conductive and mechanically stable films. Most notably, the material exhibits pronounced ORR activity and exceptional electrochemical durability in acidic media, despite the well-known tendency of Fe to dissolve under such conditions. The retention of ORR performance after prolonged cycling highlights the effectiveness of the graphitic carbon sheath and strong Fe–C interfacial interactions in suppressing Fe dissolution. These results underline a structure–stability–function relationship that is rarely demonstrated for Fe-based materials in acidic environments and point toward broader applicability in integrated electrochemical and energy-conversion devices, beyond simple activity comparisons.

4. Conclusions

Fe nanoparticle-incorporated carbon nanofibers (Fe–CNFs) were successfully synthesized through electrospinning of a ferrous acetate/PVA precursor followed by vacuum calcination at 850 °C. The combined SEM, TEM, SAED, and XRD analyses confirmed the formation of uniform nanofibers containing well-dispersed crystalline α-Fe nanoparticles embedded within a partially graphitized carbon matrix. Magnetic measurements demonstrated clear ferromagnetic behavior at both 5 K and 300 K, consistent with the presence of metallic multi-domain Fe nanoparticles.

Electrochemical evaluation demonstrated that the Fe–CNFs exhibit strong activation behavior in alkaline medium, where Fe(II)/Fe(III) redox transitions evolve into stable Fe–oxyhydroxide active sites. As a result, the catalyst displayed excellent electrocatalytic activity toward urea oxidation, achieving high current densities and negative shifts in onset potential with increasing urea concentration. In acidic media, the Fe–CNFs maintained a stable capacitive response and demonstrated pronounced oxygen reduction reaction activity. Remarkably, the material exhibited exceptional ORR durability in 0.5 M H_2SO_4, retaining its electrochemical characteristics after 300 consecutive cycles. This high acid stability—uncommon for Fe-based materials—is attributed to the protective graphitic encapsulation of Fe nanoparticles and strong Fe–C interfacial bonding that suppress dissolution. In addition to the powder form, electrospinning directly onto silicon wafers produced dense, conductive Fe–CNF films strongly adhered to the substrate, broadening the material's potential for device integration. Overall, the results highlight Fe–CNFs derived from inexpensive acetate precursors

as cost-effective, structurally robust, and electrochemically versatile materials with promising applications in electrocatalysis, wastewater-to-energy systems, magnetic devices, and integrated microelectronic platforms.

Conflicts of interest

The authors declare no conflicts of interest.

Data availability

The data supporting the findings of this study are available from the corresponding author upon reasonable request.

Acknowledgements

The authors declare that no funding was received to support this study. During the preparation of this work, the authors used ChatGPT (OpenAI) to improve grammar, clarity, and language expression. The authors reviewed and edited the content and take full responsibility for the final publication.

References

1 L. Feng, N. Xie and J. Zhong, *Materials*, 2014, **7**, 3919–3945.
2 D. Yadav, F. Amini and A. Ehrmann, *Eur. Polym. J.*, 2020, **138**, 109963.
3 J. Xue, T. Wu, Y. Dai and Y. Xia, *Chem. Rev.*, 2019, **119**, 5298–5415.
4 M. S. Islam, B. C. Ang, A. Andriyana and A. M. Afifi, *SN Appl. Sci.*, 2019, **1**, 1248.
5 K. Liu, S. Kattel, V. Mao and G. Wang, *J. Phys. Chem. C*, 2016, **120**, 1586–1596.
6 L. Wang, W. He, D. Yin, H. Zhang, D. Liu, Y. Yang, W. Yu and X. Dong, *Renewable Sustainable Energy Rev.*, 2023, **181**, 113354.
7 N. A. Barakat, A. Saadawi, K. Madih and R. Hefny, *Next Mater.*, 2025, **9**, 101036.
8 N. A. Barakat, M. T. Amen, F. S. Al-Mubaddel, M. R. Karim and M. Alrashed, *J. Adv. Res.*, 2019, **16**, 43–53.
9 T. Wang, L. Xu, C. Sun, X. Li, Y. Yan and F. Li, *RSC Adv.*, 2023, **13**, 3835–3842.
10 W. Feng, M. Liu, J. Liu, Y. Song and F. Wang, *Catal. Sci. Technol.*, 2018, **8**, 4900–4906.
11 M. Rauf, Y.-D. Zhao, Y.-C. Wang, Y.-P. Zheng, C. Chen, X.-D. Yang, Z.-Y. Zhou and S.-G. Sun, *Electrochem. Commun.*, 2016, **73**, 71–74.
12 A. Pedersen, K. Kumar, Y.-P. Ku, V. Martin, L. Dubau, K. T. Santos, J. Barrio, V. A. Saveleva, P. Glatzel and V. K. Paidi, *Energy Environ. Sci.*, 2024, **17**, 6323–6337.
13 N. A. Barakat, A. M. Tayeb, R. Hamad, M. Hashem, H. Fouad, H. Y. Kim and R. A. Hefny, *RSC Adv.*, 2024, **14**, 34904–34917.
14 N. A. Barakat, M. H. El-Newehy, A. S. Yasin, Z. K. Ghouri and S. S. Al-Deyab, *Appl. Catal., A*, 2016, **510**, 180–188.
15 J. C. De Jesus, I. González, A. Quevedo and T. Puerta, *J. Mol. Catal. A: Chem.*, 2005, **228**, 283–291.
16 M. Afzal, P. Butt and H. Ahmad, *J. Therm. Anal.*, 1991, **37**, 1015–1023.
17 N. A. Barakat, K. A. Khalil, I. H. Mahmoud, M. A. Kanjwal, F. A. Sheikh and H. Y. Kim, *J. Phys. Chem. C*, 2010, **114**, 15589–15593.
18 N. A. Barakat, M. El-Newehy, S. S. Al-Deyab and H. Y. Kim, *Nanoscale Res. Lett.*, 2014, **9**, 2.
19 N. A. Barakat, M. Motlak, A. A. Elzatahry, K. A. Khalil and E. A. Abdelghani, *Int. J. Hydrogen Energy*, 2014, **39**, 305–316.
20 T. D. Nguyen and J. S. Lee, *Appl. Sci.*, 2022, **12**, 6048.
21 N. M. Kilic, S. S. Gelen, S. Er Zeybekler and D. Odaci, *ACS Omega*, 2024, **9**, 3–15.
22 J. Xue, T. Wu, Y. Dai and Y. Xia, *Chem. Rev.*, 2019, **119**, 5298–5415.
23 X.-H. Sun, C.-P. Li, W.-K. Wong, N.-B. Wong, C.-S. Lee, S.-T. Lee and B.-K. Teo, *J. Am. Chem. Soc.*, 2002, **124**, 14464–14471.
24 B. Abolpour and R. Shamsoddini, *Prog. React. Kinet. Mech.*, 2020, **45**, 1468678319891416.
25 H. Mehrer, M. Eggersmann, A. Gude, M. Salamon and B. Sepiol, *Mater. Sci. Eng., A*, 1997, **239**, 889–898.
26 T. Gu, J. Qin, C. Xu and X. Bian, *Phys. Rev. B: Condens. Matter Mater. Phys.*, 2004, **70**, 144204.
27 U. Khalilov, G. Pourtois, S. Huygh, A. Van Duin, E. Neyts and A. Bogaerts, *J. Phys. Chem. C*, 2013, **117**, 9819–9825.
28 S. Emori and G. S. Beach, *J. Phys.: Condens. Matter*, 2011, **24**, 024214.
29 Y.-S. Meng, S.-D. Jiang, B.-W. Wang and S. Gao, *Acc. Chem. Res.*, 2016, **49**, 2381–2389.
30 S. Li, T. Zhang, R. Tang, H. Qiu, C. Wang and Z. Zhou, *J. Magn. Magn. Mater.*, 2015, **379**, 226–231.
31 L. Trotochaud, S. L. Young, J. K. Ranney and S. W. Boettcher, *J. Am. Chem. Soc.*, 2014, **136**, 6744–6753.
32 G. Mo, S. Liao, Y. Zhang, W. Zhang and J. Ye, *Electrochim. Acta*, 2012, **76**, 430–439.
33 E. M. Rodrigues, C. M. Fernandes, O. C. Alves, E. C. Santos, F. Garcia, Y. Xing, E. A. Ponzio and J. C. M. Silva, *Int. J. Hydrogen Energy*, 2024, **51**, 1460–1470.
34 K. Jian, W. Men, C. Miao, Y. Du, H. Yang and X. Zhao, *Talanta*, 2025, **292**, 127942.
35 W. Xu, D. Du, R. Lan, J. Humphreys, Z. Wu and S. Tao, *New J. Chem.*, 2017, **41**, 4190–4196.
36 G. Das, R. M. Tesfaye, Y. Won and H. H. Yoon, *Electrochim. Acta*, 2017, **237**, 171–176.
37 L. Gao, M. Xiao, Z. Jin, C. Liu, J. Zhu, J. Ge and W. Xing, *J. Energy Chem.*, 2018, **27**, 1668–1673.
38 K. Song, B. Yang, X. Zou, W. Zhang and W. Zheng, *Energy Environ. Sci.*, 2024, **17**, 27–48.
39 Y.-W. Li, W.-J. Zhang, J. Li, H.-Y. Ma, H.-M. Du, D.-C. Li, S.-N. Wang, J.-S. Zhao, J.-M. Dou and L. Xu, *ACS Appl. Mater. Interfaces*, 2020, **12**, 44710–44719.
40 D. Li, Y. Qu, X. Liu, C. Zhai and Y. Liu, *Int. J. Hydrogen Energy*, 2021, **46**, 18364–18375.
41 C. Anushree, D. N. G. Krishna, B. Lahiri and J. Philip, *J. Phys. Chem. C*, 2020, **124**, 5702–5714.